GEOSPHERE

GEOSPHERE, v. 14, no. 1

doi:10.1130/GES01570.1

8 figures; 2 tables; 1 supplemental file

CORRESPONDENCE: gljhg@bristol.ac.uk; j.gottsmann@bristol.ac.uk

CITATION: Gottsmann, J., del Potro, R., and Muller, C., 2017, 50 years of steady ground deformation in the Altiplano-Puna region of southern Bolivia: Geosphere, v. 14, no. 1, doi:10.1130/GES01570.1.

Science Editor: Raymond M. Russo
Guest Associate Editor: Matthew Pritchard

Received 11 June 2017
Revision received 18 August 2017
Accepted 9 October 2017

50 years of steady ground deformation in the Altiplano-Puna region of southern Bolivia

Joachim Gottsmann[1], Rodrigo del Potro[1], and Cyril Muller[2]

[1]School of Earth Sciences, University of Bristol, Bristol BS8 1RJ, UK
[2]Observatorio Vulcanologico y Sismologico de Costa Rica, Universidad Nacional, 2346-3000 Heredia, Costa Rica

ABSTRACT

The Altiplano-Puna Volcanic Complex of the Central Andes is host to an ~150-km-wide, quasi-circular ground deformation anomaly centered on Uturuncu volcano (Bolivia). The precise onset and duration of this deformation is unclear, but geomorphologic studies bracket its initiation at less than a few hundred years ago. Here we report on the deformation history over an ~50 yr period by deriving orthometric height changes from leveling and global navigation satellite system (GNSS) observations at 53 benchmarks along a regional leveling line that crosses the deformation anomaly. The comparison of interferometric synthetic aperture radar (InSAR) line-of-sight (LOS) displacements and LOS-projected orthometric ground velocities in a common reference frame reveal central uplift extending to ~35 km from Uturuncu at a maximum orthometric rate of 1.2 cm yr^{-1}, and peripheral subsidence at a maximum rate of 0.3 cm yr^{-1} to ~60 km from Uturuncu. This pattern is consistent with the spatial extent and average rate of deformation observed by InSAR. Our interpretation of the data is that long-wavelength ground uplift at Uturuncu has likely occurred at a quasi-constant rate for at least half of a century. This study bridges the observational time spans between modern satellite geodetic observations (up to a few decades) and geomorphological observations (a few centuries and longer) of the recent deformation history of the continental crust in the Central Andes and adds to a select group of case studies of quantifiable long-term volcano deformation worldwide.

INTRODUCTION

Satellite remote sensing techniques documented an unusually wide and spatially complex ground deformation in the Altiplano-Puna Volcanic Complex (de Silva, 1989) between A.D. 1992 and 2011 (e.g., Pritchard and Simons, 2002; Henderson and Pritchard, 2013; Fialko and Pearse, 2012) (Fig. 1), with a diameter of 150 km, a peripheral moat of subsidence, and a central area undergoing uplift at rate of up to 1 cm yr^{-1} at the western slopes of Uturuncu volcano (Bolivia; 22.270°S, 67.180°W) as detected in interferometric synthetic aperture radar (InSAR) line-of-sight (LOS) displacement data. The spatially and temporally complex deformation may be linked with an ~200-km-wide

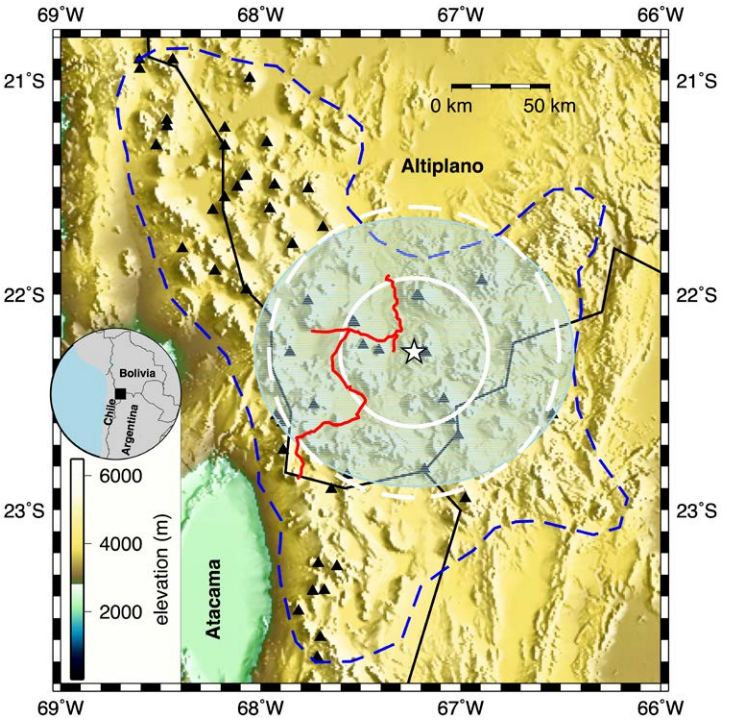

Figure 1. Overview map of the Altiplano-Puna region of southern Bolivia. White star (22.270°S, 67.233°W) marks the maximum uplift of ~1 cm/yr^{-1} as detected by interferometric synthetic aperture radar (InSAR) line-of-sight measurements (Henderson and Pritchard, 2017), located on the western slope of Uturuncu volcano. Spatial extent of the uplifting region, determined to have a radius of ~40 km from InSAR data, is marked by a white solid circle. Peripheral subsidence, between ~40 and ~70 km distance, is shown by the white dashed circle. Dashed blue line outlines the spatial extent of the Altiplano-Puna Volcanic Complex (de Silva, 1989). The spatial extent of the 2.5 km s^{-1} velocity contour of the S-wave velocity model of the Altiplano-Puna magma body at 20 km below sea level presented by Ward et al. (2014) is shown by the light-green transparent ellipse and is similar in size to the footprint of the InSAR anomaly. Black solid lines mark international borders; black triangles mark volcanic centers of the Altiplano-Puna Volcanic Complex. Red line shows the original leveling line (line BP), established in 1965. Elevations in the digital elevation model are given in meters above sea level.

and ~11-km-thick geophysically anomalous upper-crustal magma reservoir—the Altiplano-Puna magma mush or magma body (Fig. 1) (Zandt et al., 2003; Fialko and Pearse, 2012; Comeau et al., 2016; Gottsmann et al., 2017). This reservoir is imaged with a volume of 300,000 km^3 and is thought to contain up to 25 vol% of wet andesitic melt (Laumonier et al., 2017; Ward et al., 2014).

Situated in a large Neogene ignimbrite province where a total of >15,000 km^3 of ignimbrites have been erupted over the past 15 m.y. (e.g., Salisbury et al., 2011; Kern et al., 2016), Uturuncu volcano ceased its eruptive activity ~250 k.y. ago (Muir et al., 2015; Sparks et al., 2008) and must hence be deemed extinct. However, this Pleistocene volcano shows signs of unrest with summit fumarolic activity and its western flank in the center of the uplift area. Therefore, questions remain as to the possibility of a future renewal of eruptive activity at Uturuncu volcano and the Altiplano-Puna Volcanic Complex as a whole, particularly in light of a substantial volume of melt stored within the Altiplano-Puna magma body.

While satellite remote sensing and ground-based observation only provide a temporally narrow window of opportunity to investigate this large-scale crustal deformation, geomorphic investigations have extended the window to time scales of hundreds to thousands of years. The main finding from these studies is that the observed deformation has been ongoing for no more than ~100 yr (Perkins et al., 2016), leading to the conclusion that the current deformation can be regarded as a result of transient changes in the crustal stress conditions beneath the Altiplano-Puna Volcanic Complex (Gottsmann et al., 2017). There is hence a disconnect between the annual time scale of global navigation satellite system (GNSS) observations, the decadal time scale of InSAR observations, and the time scale of geomorphic observations as to the longevity of this transient deformation and its time of onset. In contrast, a similar long-wavelength (~100-km-wide) surface deformation pattern (i.e., central uplift and peripheral subsidence) with a near-constant uplift of 0.2 cm yr^{-1} above the Socorro magma body in New Mexico, USA (Finnegan and Pritchard, 2009; Pearse and Fialko, 2010), has been documented geodetically for >100 yr and provides a rare glimpse into the time scales and rates of large-scale deformation from magmatic processes in the continental crust.

The purpose of this paper is to improve our understanding of the duration, wavelength, and magnitude of the ongoing deformation in the Altiplano-Puna Volcanic Complex by combining leveling data collected in 1965 with new GNSS survey data. We expect this research to inform future studies into the cause of the deformation, its spatio-temporal evolution, and likely future evolution.

DATA AND METHODS

Leveling Survey

We have retrieved data from the Bolivian geographical survey (Instituto Geográfico Militar de Bolivia) from one geodetic leveling line (termed BP), which were measured in 1965 west of Uturuncu in the Bolivian Altiplano region (Fig. 1). With a line length of 205 km, the original spacing of the benchmarks along BP was between 1 and 3 km. The line is classified as a first-order survey, implying that data were measured with an overall vertical accuracy of <7 cm, given by 0.5 cm × $L^{1/2}$, for a class II survey, where L is the length of the survey in kilometers (Vanicek et al., 1980). Our initial field inspection in 2010 found that 53 original benchmarks along BP remained unaltered and undisturbed and fit for measuring. The rest of them were either slightly damaged, completely destroyed, or buried, i.e., deemed unfit for measuring. Figure 2 shows the spatial extent of the main BP line and its branch lines within the deformation anomaly detected in the InSAR data.

GNSS and Gravity Surveys

We obtained dual-frequency GNSS measurements in rapid-static survey mode at 53 healthy benchmarks along line BP in 2011–2012 (Table 1; Fig. 2). The first benchmark we measured is BP07, located to the north of Uturuncu volcano and a distance of 12.4 km from the start of the original BP line. From BP07, we measured a number of healthy benchmarks running south toward Uturuncu and along the road running west toward Laguna Colorada. A long segment of BP runs along a fringe of the InSAR-detected deformation anomaly (Fig. 2B), so little information on spatial deformation changes can be gleaned from that segment. We measured only two points in this segment (BP48 and BP57), and then continued with the more systematic measurements starting from BP69A with an average point spacing of 2 km. From there, the leveling line runs radially away from Uturuncu toward the southwest and reaches the border with Chile (BP100G), across and past the far side of the peripheral subsidence as identified by InSAR. Benchmark identifiers and coordinates are given in Table 1 and in the Supplemental File[1].

We measured positions of benchmarks using dual-frequency Leica 1200 GNSS receivers and antennas. We used between three and six known GNSS bases located at a maximum distance of 100 km, recording between 20 min and several hours with a recording interval of 3–30 s, depending on the distance to the base stations used. Data were processed using Leica Geo Office and TopCon Tools software (http://leica-geosystems.com/en-gb/products/total-stations/software/leica-geo-office; http://www.topconcare.com/en/software/office-applications/topcon-tools-8/), and phase ambiguities were solved in every case, to achieve a vertical GNSS repeatability of <5 cm. We also took relative gravity measurements at most benchmarks using a Scintrex CG5 Autograv (serial number 572) as part of a larger survey (del Potro et al., 2013). For BP07 to BP14, BP16 to BP21, and BP35, where gravity was not measured on the benchmark, gravity values were extrapolated by a distance-weighted average of measurements done on nearby locations on either side of the BP benchmarks along the same road. These gravity values were reduced by taking into account the elevation difference between the benchmarks and a Bouguer slab density of 2270 kg m^{-3} (see del Potro et al., 2013).

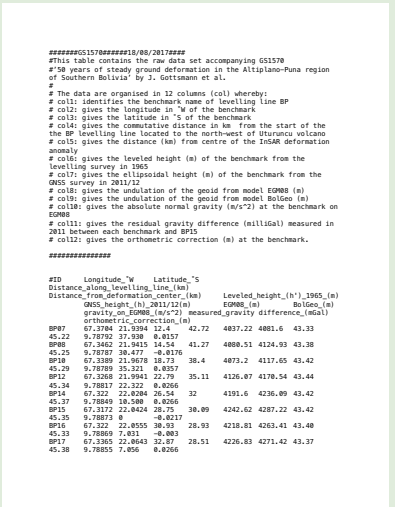

```
#######GS1570######18/08/2017####
#This table contains the raw data set accompanying GS1570
#'50 years of steady ground deformation in the Altiplano-Puna region
of Southern Bolivia' by J. Gottsmann et al.
#
# The data are organised in 12 columns (col) whereby:
# col1: identifies the benchmark name of levelling line BP
# col2: gives the longitude in °W of the benchmark
# col3: gives the latitude in °S of the benchmark
# col4: gives the commutative distance in km  from the start of the
the BP levelling line located to the north-west of Uturuncu volcano
# col5: gives the distance (km) from centre of the InSAR deformation
anomaly
# col6: gives the leveled height (m) of the benchmark from the
levelling survey in 1965
# col7: gives the ellipsoidal height (m) of the benchmark from the
GNSS survey in 2011/12
# col8: gives the undulation of the geoid from model EGM08 (m)
# col9: gives the undulation of the geoid from model BolGeo (m)
# col10: gives the absolute normal gravity (m/s^2) at the benchmark on
EGM08
# col11: gives the residual gravity difference (milliGal) measured in
2011 between each benchmark and BP15
# col12: gives the orthometric correction (m) at the benchmark.

##############


#ID     Longitude_°W    Latitude_°S
Distance_along_levelling_line_(km)
Distance_from_deformation_center_(km)      Leveled_height_(h')_1965_(m)
          GNSS_height_(h)_2011/12(m)       EGM08_(m)       BolGeo_(m)
          gravity_on_EGM08_(m/s^2) measured_gravity difference_(mGal)
          orthometric_correction_(m)
BP07      67.3704  21.9394  12.4     42.72    4037.22  4081.6   43.33
45.22     9.78792  37.930   0.0157
BP08      67.3462  21.9415  14.54    41.27    4080.51  4124.93  43.38
45.25     9.78787  30.477   -0.0176
BP10      67.3389  21.9678  18.73    38.4     4073.2   4117.65  43.42
45.29     9.78789  35.321   0.0357
BP12      67.3268  21.9941  22.79    35.11    4126.07  4170.54  43.44
45.34     9.78817  22.322   0.0266
BP14      67.322   22.0204  26.54    32       4191.6   4236.09  43.42
45.37     9.78849  10.500   0.0266
BP15      67.3172  22.0424  28.75    30.09    4242.62  4287.22  43.42
45.35     9.78873  0        -0.0217
BP16      67.322   22.0555  30.93    28.93    4218.81  4263.41  43.40
45.33     9.78869  7.031    -0.003
BP17      67.3365  22.0643  32.87    28.51    4226.83  4271.42  43.37
45.38     9.78855  7.056    0.0266
```

[1]Supplemental File. Benchmark locations, geoid undulations, and gravity data (text file). Please visit http://doi.org/10.1130/GES01570.S1 or the full-text article on www.gsapubs.org to view the Supplemental File.

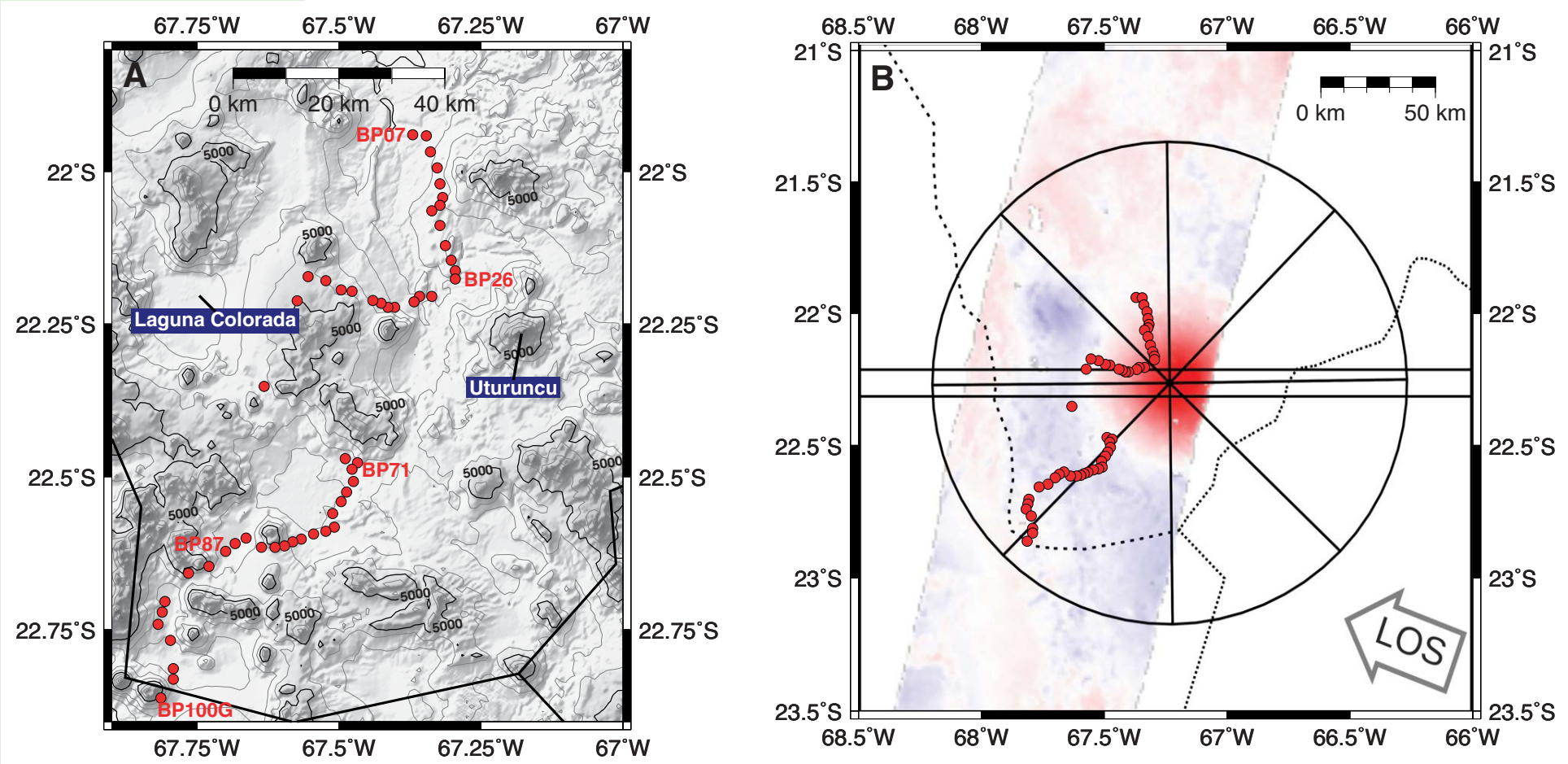

Figure 2. (A) Map showing benchmark locations along the main BP leveling line measured in this study, Altiplano-Puna region, southern Bolivia. Labeled contours indicate elevation in meters above sea level. (B) Location of the BP line within the quasi-axisymmetric interferometric synthetic aperture radar (InSAR) deformation anomaly recorded between 1992 and 2011; Henderson and Pritchard, 2017). Hot colors indicate uplift with maximum magnitude of 1 cm yr^{-1}; cold colors represent subsidence at maximum magnitude of 0.2 cm yr^{-1}. Lines intersecting at the center of the anomaly show the location of profiles used to depict average interferometric synthetic aperture radar (InSAR) line-of-sight (LOS) ground velocity data shown in Figure 8. Horizontal black lines show the location of the east-west swath profile used to determine vertical and radial components of InSAR-detected deformation shown in Figure 7. Dotted lines mark international borders.

TABLE 1. BENCHMARK LOCATIONS ALONG LEVELING LINE BP, ALTIPLANO-PUNA REGION, SOUTHERN BOLIVIA

BM ID	Longitude (°W)	Latitude (°S)	Dist. BP (km)	Dist. InSAR (km)	*h* (m)
BP07	67.3704	21.9394	12.4	42.52	4081.60
BP08	67.3462	21.9415	14.54	41.02	4124.93
BP10	67.3389	21.9678	18.73	38.16	4117.65
BP12	67.3268	21.9941	22.79	33.88	4170.54
BP14	67.322	22.0204	26.54	31.82	4236.09
BP15	67.3172	22.0424	28.75	29.93	4287.22
BP16	67.322	22.0555	30.93	28.83	4263.41
BP17	67.3365	22.0643	32.87	28.49	4271.42
BP19	67.322	22.0884	36.72	25.39	4313.84
BP21	67.3123	22.1213	40.93	22.03	4394.58
BP23	67.3026	22.1454	44.57	19.27	4351.23
BP24	67.2954	22.1629	46.73	17.77	4284.53
BP26	67.2954	22.1761	49.57	16.54	4190.62
BP31	67.3365	22.2047	57.6	18.65	4275.09
BP32	67.3583	22.2047	59.63	20.45	4252.06
BP33	67.368	22.2135	61.27	21.18	4306.82
BP35	67.4019	22.2224	64.91	23.97	4477.89
BP36	67.414	22.2224	66.46	25.3	4562.37
BP37	67.4261	22.2159	68.1	26.67	4610.14
BP38	67.4406	22.2115	69.87	28.26	4656.12
BP40	67.477	22.1962	73.71	31.92	4733.04
BP41	67.4963	22.1941	75.67	33.47	4771.37
BP43	67.523	22.1788	79.44	36.55	4837.38
BP45	67.5544	22.1723	82.59	39.6	4878.89
BP48	67.5738	22.2118	88.14	40.7	4996.06
BP57	67.6319	22.3523	105.18	46.96	4750.22
BP69A	67.4891	22.4704	132.31	39.76	4476.26
BP69B	67.4673	22.4769	134.01	38.91	4481.88
BP71	67.477	22.4879	134.71	40.1	4458.20
BP72	67.4745	22.5076	137.12	41.39	4451.47
BP73	67.4866	22.5252	139.16	43.32	4441.17
BP74	67.4963	22.5406	141.29	45.4	4443.38
BP75	67.5109	22.5604	143.35	47.18	4452.10
BP77	67.5084	22.5823	147.17	49.28	4449.43
BP78	67.523	22.5889	149.13	51	4450.26
BP79	67.5448	22.5933	151.22	52.99	4466.02
BP80	67.5665	22.6022	153.25	54.89	4525.97
BP81	67.5811	22.6066	155	56.46	4619.80
BP82	67.5956	22.6132	156.68	57.94	4721.98
BP83	67.6125	22.6154	158.55	59.39	4775.99
BP84	67.6368	22.6155	160.43	60.62	4756.39
BP86	67.6634	22.6002	164.02	62.17	4553.86
BP87	67.6828	22.609	166.1	64.06	4499.84
BP88	67.6997	22.6222	168.19	66.07	4531.68
BP90	67.7288	22.6464	172.35	69.98	4593.28
BP92	67.7651	22.6574	176.25	73.48	4772.22
BP96	67.8063	22.7036	184.4	80.5	4506.96
BP97	67.8111	22.7211	186.56	81.88	4471.60
BP98	67.8184	22.7409	188.74	83.49	4432.43
BP100	67.7966	22.7671	193.13	84.06	4382.41
BP100C	67.7917	22.8132	198.98	87.06	4375.32
BP100D	67.7917	22.8307	201.28	88.74	4438.15
BP100G	67.8135	22.8615	204.74	93.05	4520.73

Note: BM ID—benchmark identifier; Dist. BP—distance along main leveling line; Dist. InSAR—distance along an east-to-west radial profile from the center of deformation detected in interferometric synthetic aperture radar (InSAR) data; *h*—ellipsoidal heights of benchmarks along line BP shown in Fig. 2A.

To set an absolute reference for the gravity measurements, we chose an arbitrary benchmark (BP15) where gravity was measured during the survey, and used the gravity value on the geoid using model EGM2008 (g_{oBP15} = 9.7887 m s^{-2}) to calculate the absolute gravity on the benchmark (g_{BP15}) using the simplified Poincaré-Prey reduction (Hofmann-Wellenhof and Moritz, 2005) for an average crustal density of 2670 kg m^{-3}:

$$g_{BP15} = g_{oBP15} + 0.848 \times 10^{-6} \times H_{BP15}, \quad (1)$$

where H_{BP15} is the orthometric height of BP15 (see below for calculation of orthometric heights). We use the so-derived value g_{BP15} = 9.7923 m s^{-2} as a reference for all relative gravity values measured in the survey. This procedure does not affect the gravity change values along the leveling line relative to BP15. See Table 2 for a list of notations used in this study.

Conversion to Orthometric Heights

GNSS data cannot be directly compared with leveled heights. The former provide Cartesian (XYZ) solutions that do not express a notion of elevation above a certain datum, whereas the latter depend on the geopotential surface along the path followed (Fig. 3). To permit direct comparison, both data sets must be converted to orthometric heights.

First, GNSS solutions are transformed into geodetic latitude, longitude, and ellipsoidal heights using the WGS84 ellipsoid model (Hofmann-Wellenhof and Moritz, 2005). Ellipsoidal heights (*h*) are then converted to (approximate) orthometric heights (*H*) by means of the geoid undulation (*N*; Figs. 3 and 4) (Hofmann-Wellenhof and Moritz, 2005) using:

$$H \approx h - N. \quad (2)$$

TABLE 2. SYMBOLS AND NOTATIONS USED IN THIS STUDY

Notation or symbol	Description	Value or units
γ_0	Theoretical value of gravity at 22°S	m s^{-2}
g	Gravity at observation point	m s^{-2}
Δg	Measured difference in gravity between two benchmarks	mGal
g_{oBP15}	Theoretical gravity on geoid at benchmark BP15 used as absolute reference (see Equation 1 in text)	9.7887 m s^{-2}
h'	Leveled height of benchmark	m
$\Delta h'$	Leveled height difference between two benchmarks	m
h	Ellipsoidal height of benchmark	m
H	Orthometric height of benchmark	m
N	Geoid undulation (see Fig. 4 in text)	m
OC	Orthometric correction (see Equation 3 in text)	m
k	Vertical offset between $LOS_{\Delta H}$ and LOS_{InSAR}	m
LOS_{InSAR}	Deformation observed in interferometric synthetic aperture radar (InSAR) line-of-sight (LOS) data	m
$LOS_{\Delta H}$	Orthometric height change of benchmark projected onto the InSAR LOS	m

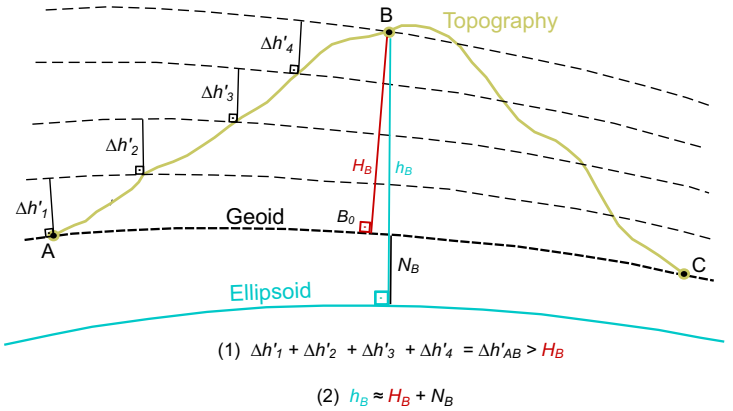

Figure 3. Schematic diagram illustrating reconciliation of leveled, orthometric, and ellipsoidal heights between two benchmarks, A and B, along geopotential surfaces (black stippled lines). Leveling increments ($\Delta h'$) from level measurements at a set of intermediate points are summed to determine the difference in leveled height ($\Delta h'_{AB}$) and are converted to orthometric height differences (ΔH_{AB}) by adding an orthometric correction (see Equation 3 and text). In the example, geoid undulation N_B is subtracted from ellipsoidal heights h_B determined from global navigation satellite system (GNSS) measurements to obtain orthometric height H_B (cf. Equation 2).

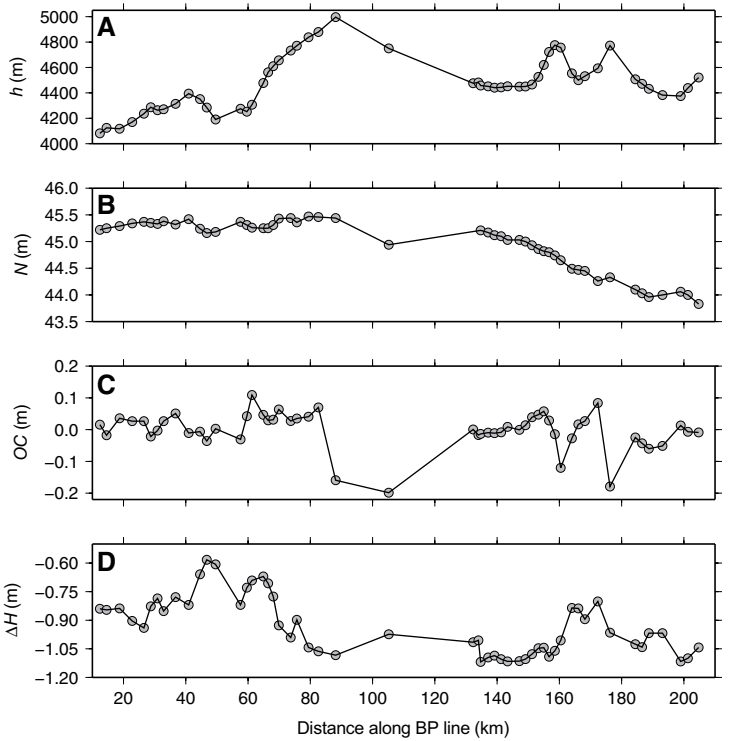

Figure 4. Geodetic parameters as a function of distance along leveling line BP running north-south (see Fig. 2) and derived orthometric height changes, Altiplano-Puna region, southern Bolivia. (A) Ellipsoidal heights of benchmarks. (B) Undulations (N) of geoid model BOLGEO (Corchete et al., 2006). (C) Orthometric correction (OC) applied to each benchmark according to Equation 3. (D) Derived orthometric height changes (ΔH) between 1965 and 2012.

For this we have used the national geoid model BOLGEO (Corchete et al., 2006) (Fig. 4 and the Supplemental File [footnote 1]), which provides better accuracy compared to a global model such as EGM2008. EGM2008 and BOLGEO can be reconciled by adding a vertical offset of 2.2 m to EGM2008.

Because of the nonparallelism of geopotential (level) surfaces, elevations of benchmarks from spirit leveling are not only different from heights above the geoid (such as orthometric heights) but also ambiguous; i.e., they are path dependent (Hofmann-Wellenhof and Moritz, 2005). Level heights (h') must hence be converted to orthometric heights (H) (see Fig. 3). This is done by adding an orthometric correction (OC) to h'. Because we do not know the datum for the leveled heights, orthometric corrections are given relative to the previous point measured along the line. The correction between two benchmarks on the Earth's surface, A and B, is given by (Hofmann-Wellenhof and Moritz, 2005):

$$OC_{AB} = \sum_{A}^{B} \frac{g-\gamma_0}{\gamma_0}\Delta h' + \frac{\bar{g}_A-\gamma_0}{\gamma_0}h'_A - \frac{\bar{g}_B-\gamma_0}{\gamma_0}h'_B, \quad (3)$$

where γ_0 is the theoretical (normal) gravity calculated for 22.26°S latitude (9.784 m s^{-2}), g is the gravity determined at the level points between A and B, and $\Delta h'$ is the leveling increment. h'_A and h'_B are the leveled heights of points A and B respectively (see Supplemental File [footnote 1]). $\bar{g}_A$ and $\bar{g}_B$ are the mean val-

ues of gravity along the plumb lines between the geoid and benchmarks A and B and are calculated as the arithmetic mean of g at the level points and their respective gravity on the geoid g_o (using a simplified Poincaré-Prey reduction) (Hofmann-Wellenhof and Moritz, 2005):

$$\bar{g} = 1/2\ (g + g_o), \tag{4}$$

$$\bar{g} = g + 0.424 \times 10^{-6} \cdot h'. \tag{5}$$

Because in most cases there were no gravity measurements taken between BP benchmarks, the summation of g was simplified to the average of gravity measured at two consecutive benchmarks.

RESULTS

The two sets of orthometric heights, derived from leveling and GNSS observations, are compatible and thus comparable (see Supplemental File [footnote 1]). Derived orthometric height changes between 1965 and 2012 along the main leveling line vary between –0.60 m and –1.15 m and are shown in Figure 4D. The constant offset is a combination of datum offsets, the choice of reference gravity, and the vertical movement of the entire region between 1965 and 2012. This implies a maximum relative height change along the leveling line of 0.55 m between the two surveys. We can derive the spatial deformation pattern from the orthometric height differences over 47 yr by plotting the differences along a radial westward trajectory from the center of the InSAR anomaly (Fig. 5).

The orthometric height change pattern shows relative uplift of up to 45 cm in the area of ground inflation detected by InSAR to a radial distance of ~40 km. From there, up to 15 cm of subsidence are observed over 20 km, which coincides with an area where InSAR data show the start of an ~20-km-wide area of LOS subsidence. The resultant orthometric deformation pattern is hence similar to the spatial deformation pattern derived from 18 yr of InSAR observations in terms of relative magnitude, wavelength, and position of areas of uplift and subsidence.

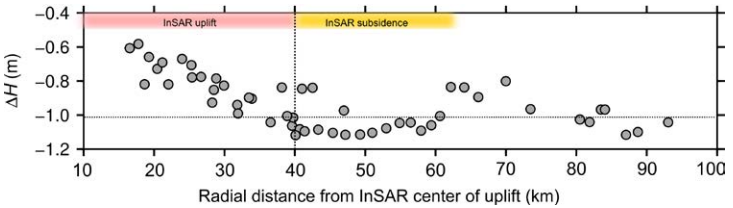

Figure 5. Orthometric height changes (ΔH) between 1965 and 2012 as a function of radial distance from the center of the deformation anomaly observed in interferometric synthetic aperture radar (InSAR) data. Areas of uplift and subsidence as detected by InSAR are shown for reference. Horizontal stippled line marks a tentative line of zero net deformation based on InSAR observations. Note that the ΔH data have not been georeferenced for direct comparison with InSAR-detected deformation. See text for details.

DISCUSSION

The absence of a common datum for the InSAR and orthometric deformation data introduces an unknown vertical offset between them. To address this, one possible solution is to assume that a given point has not moved at all, whereby $\Delta H = 0$; one then uses that point as an arbitrary anchor between the two surveys. A different approach, followed here, is to use the known deformation trend from 18 yr of InSAR observations as a calibration to test whether the deformation patterns are indeed comparable and can be used to inform the deformation history since 1965. This calibration, however, has to be done with care, as both orthometric height change and InSAR LOS displacement are one-dimensional measurements of the true three-dimensional (3-D) displacement (Fig. 6). Changes in orthometric height (ΔH) represent the vertical component (u_z) of the true three-component displacement vector, while InSAR LOS displacement data give the projection of the true displacement vector onto the satellite LOS.

Comparison of Orthometric Height Changes to InSAR-Observed Deformation

As shown in Figure 6, given a true displacement vector v_A of benchmark BP_A, composed of both upward (u_z) and westward (u_r) components (whereby $u_z = u_r$ in the case shown), the change in orthometric height (ΔH_A) does not equal the change in InSAR LOS (LOS_{InSAR}). This is also true if ΔH_A is projected

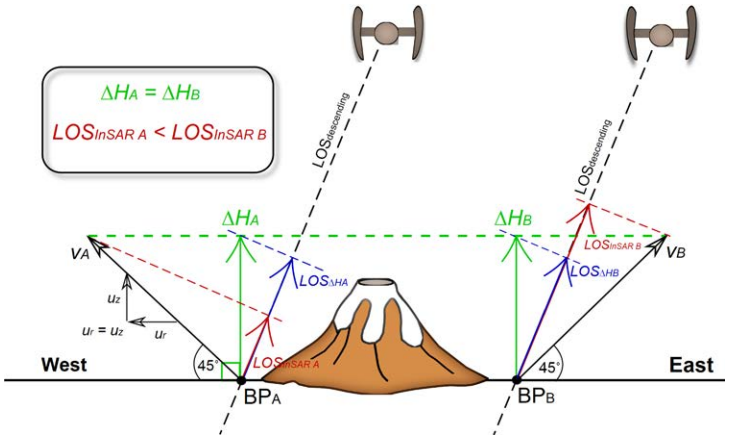

Figure 6. Schematic diagram of the interpretation of differences between displacements detected in descending interferometric synthetic aperture radar (InSAR) line-of-sight (LOS) data ($LOS_{descending}$) and orthometric height changes (ΔH_A and ΔH_B) determined from leveling and GNSS data for eastward and westward displacements of virtual benchmarks BP_A and BP_B. While the magnitudes of eastward and westward displacements at BP_A and BP_B (v_A and v_B) are equal, the magnitudes of resultant InSAR LOS displacements ($LOS_{InSAR\ A}$ and $LOS_{InSAR\ B}$) are different. The illustration depicts the case of equal radial (u_r) and vertical (u_z) displacements of BP_A and BP_B. Figure is not to scale.

onto the InSAR LOS ($LOS_{\Delta HA}$). The mismatch between the orthometric deformation and InSAR-observed deformation becomes smaller for deformation dominated by vertical movement, but larger where horizontal deformation dominates. Moreover, two different 3-D displacement vectors, v_A and v_B measured at BP_A and BP_B, respectively, can yield the same magnitude of orthometric deformation $\Delta H_{A,B}$ if projected onto the InSAR LOS ($LOS_{\Delta HA,B}$) despite drastically different magnitudes of InSAR LOS displacement. This is due to the direction of the horizontal deformation component relative to the satellite's LOS with an incidence angle of 22° for the available descending InSAR tracks (Henderson and Pritchard, 2017).

Projecting Orthometric Displacements onto InSAR LOS

The BP benchmarks located within the uplifting part of the InSAR anomaly (BP12 to BP37) are located northwest of Uturuncu. Assuming that the horizontal component of the deformation is radially away from Uturuncu, the east-west component of the deformation for a descending radar track that illuminates the area from the east would contribute to the lengthening of the radar path and yield a smaller magnitude in the InSAR LOS displacement compared with the magnitude of the projected orthometric height change ($LOS_{\Delta H}$) (see Fig. 6).

We use the orthometric vertical displacements for each benchmark to project them into the InSAR LOS and derive a set of synthetic $LOS_{\Delta H}$ displacements that would arise from a perfectly radially symmetric uplift pattern such as one caused, e.g., by a buried pressurized sphere. Then we use the available InSAR LOS displacements data to help determine the magnitude of the vertical offset k in the orthometric height changes (ΔH) if projected onto the InSAR LOS, whereby:

$$k = LOS_{InSAR} - w \times LOS_{\Delta H}, \quad (6)$$

in order to obtain LOS displacements in a common reference frame. Note that the magnitude of $LOS_{\Delta H}$ is modulated by parameter w whose value is dependent on the magnitude of radial displacement (u_r) relative to the magnitude of vertical displacement (u_z) at the leveling benchmarks. For example, for $u_r/u_z = 0$ (i.e., only vertical displacement and no radial displacement), $w = 1$ and $k = LOS_{InSAR} - LOS_{\Delta H}$. For $u_r/u_z = 1$ (i.e., $u_r = u_z$), $w = 0.4$ and $k = LOS_{InSAR} - 0.4 \times LOS_{\Delta H}$.

In the above analysis, we limit the parameter space exploration of u_r/u_z to values up to 1, because a strong horizontal component acting radially from the center of the deformation would cause a horizontally elongated InSAR deformation pattern. This is inconsistent with the large-scale concentric InSAR pattern observed to date (e.g., Henderson and Pritchard, 2017).

Derivation of Deformation Velocities between 1965 and 2012

Using u_r and u_z data from an inversion of four overlapping InSAR tracks (Henderson and Pritchard, 2017), we find that u_r/u_z ratios are between –0.05 and 0.25 over a distance of ~60 km from the center of the InSAR uplift (Fig. 7A). According to Figure 7B, w hence takes values between 0.9 and 1.

The resultant vertical offset k from Equation 6 obtained by a residual minimization procedure is 2.0 ± 0.05 cm yr^{-1}, or 94 ± 2.4 cm over 47 yr. Note, that this extrapolation assumes a constant linear evolution of the deformation between 1965 and 2012.

Adding the offset to the above LOS-projected orthometric height differences, we derive the spatial ground velocity pattern shown in Figure 8. This pattern is remarkably similar to the spatial deformation pattern from 18 yr of InSAR observations in terms of magnitudes and wavelengths of both inflation and subsidence. This implies that the uplift rate recorded along the leveling line running north-south toward Uturuncu (benchmarks BP12 to BP26) is equal

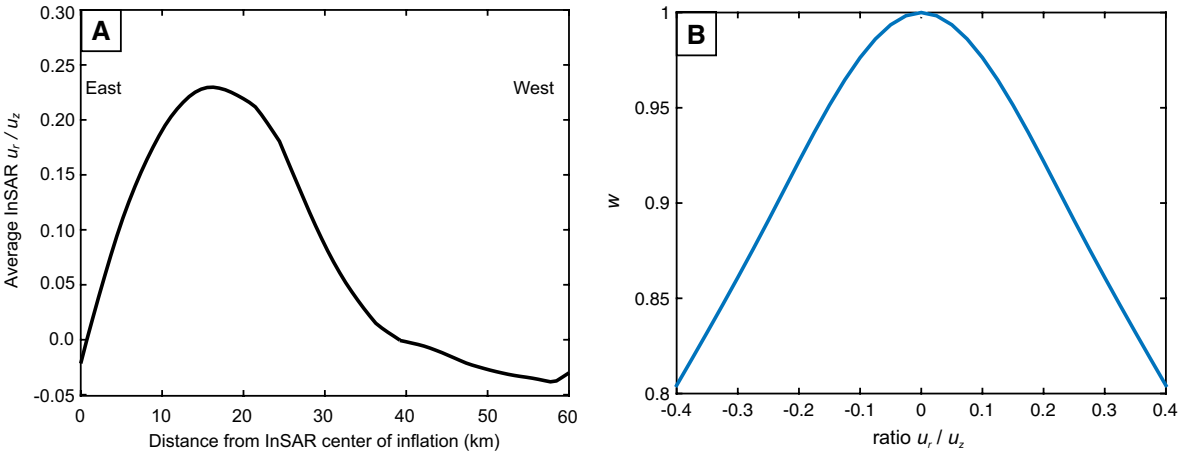

Figure 7. (A) Ratios of radial to vertical displacements u_r/u_z as a function of distance from the center of uplift derived from interferometric synthetic aperture radar (InSAR) deformation data presented by Henderson and Pritchard (2017). (A) Parameter w as a function of selected u_r/u_z ratios to convert the magnitudes of the projected orthometric height changes ($LOS_{\Delta H}$) data for the ratios shown in A according to Equation 6.

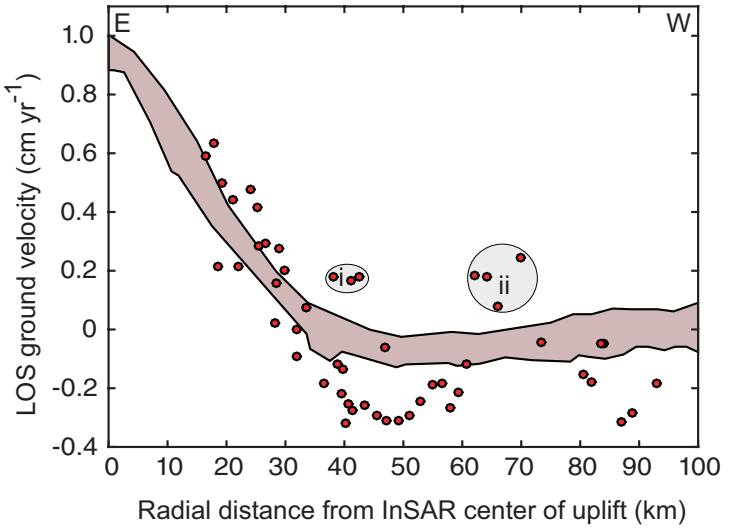

Figure 8. Comparison of line-of-sight (LOS) ground velocities from interferometric synthetic aperture radar (InSAR) (brown shading encompasses data from profiles shown in Fig. 2; data from Henderson and Pritchard, 2017) and orthometric measurements (red dots) along a radial trajectory from the center of maximum InSAR deformation westwards, Altiplano-Puna region, southern Bolivia. Orthometric height changes have been projected onto the InSAR LOS data, shifted by best-fit offset *k* (see Equation 6) and linearly averaged over a 47 yr observation period. The orthometric subsidence velocities have a higher magnitude than those detected by InSAR, which is likely due to an observation bias of InSAR data for subsidence west of Uturuncu volcano for descending radar tracks. The orthometric data identify anomalous uplift at the start of the leveling line to the northwest of Uturuncu (i) and near the active volcanic chain close to the Chilean border (ii).

to that recorded along the east-west segment (BP32 to BP45), suggesting that the vertical deformation is indeed radially symmetric from Uturuncu. A deformation source that causes a radially symmetric deformation pattern can hence reasonably explain the observations.

Extrapolating the $LOS_{\Delta H}$ ground velocities to the center of the uplift observed by InSAR and accounting for uncertainties in the derivation of velocities, we propose a maximum velocity $LOS_{\Delta H}$ of 1.1 ± 0.2 cm yr^{-1} . These values are within the uncertainty of maximum InSAR LOS ground velocities of 1.05 ± 0.07 cm yr^{-1}. The orthometric uplift extends ~35 km from Uturuncu, and peripheral subsidence, at a maximum rate of ~0.3 ± 0.03 cm yr^{-1}, extends to ~60 km from Uturuncu. The fact that the leveling line crosses the moat of subsidence to the west of the center of deformation, where InSAR observations are less reliable to detect the true magnitude of ground deflation, allows us to confirm that subsidence has indeed occurred albeit at slightly higher mean velocities than inferred from InSAR measurements.

The consistency of the spatial pattern and ground velocities between the orthometric and InSAR deformation data indicates that the long-wavelength deformation may have been constant for at least 47 yr (1965–2012). This allows us to suggest a near-constant deformation of the Altiplano-Puna Volcanic Complex over decadal time scales under the assumption that this is not a coincidence of the discrete sampling in time (1965, 1992, 2010–2011) of an oscillatory inflation-deflation process. Deriving mean velocities over such time scales from only two surveys is inherently problematic. Currently, we have no means to test our hypothesis due to the absence (to the best of our knowledge) of additional geodetic data over the same period. However, continuous GNSS observations near the center of uplift observed by InSAR indicate that the recent rate of uplift dropped to an average of 0.24 ± 0.19 cm yr^{-1} between 2010 and 2016 (Blewitt et al., 2016), similar to the long-term average detected above the Socorro magma body (Finnegan and Pritchard, 2009). Whether this uplift will continue to decelerate or accelerate again in the future remains to be seen. Either behavior has implications for the assessment of causative processes behind the complex spatio-temporal deformation. Their discussion is beyond the scope of this paper, and we refer interested readers to Gottsmann et al. (2017) where some of the implications of nonlinear history of the deformation anomaly are considered.

CONCLUSIONS

Leveling and GNSS data collected in 1965 and 2012, respectively, have allowed us to convert deformation data into orthometric height changes along a leveling line that crosses the 150-km-wide deformation anomaly centered on Uturuncu. Due to the absence of a common geodetic datum for the orthometric and InSAR displacement data, the two data sets cannot be directly compared. However, we obtain a reasonable match between the two data sets by projecting the orthometric height changes into the InSAR LOS and applying a vertical offset of 94.0 ± 2.4 cm over the 47 yr to the orthometric height changes. The ground deformation velocity pattern from 1965 to 2012 is equivalent to that observed by InSAR surveys between 1992 and 2011. We therefore propose a near-constant long-term pattern of ground deformation between 1965 and 2012 with central maximum orthometric uplift at 1.2 ± 0.2 cm yr^{-1} and maximum peripheral subsidence at 0.3 ± 0.03 cm yr^{-1} over the 150-km-wide deformation anomaly. This study adds to a select group of long-term geodetic investigations that quantitatively document protracted periods of complex spatio-temporal deformation in volcanic terrain (e.g., Finnegan and Pritchard, 2009; Parker et al., 2014). Exploitation of these data should improve our understanding of the link between protracted crustal stress changes and decadal time scales of magma transfer and reservoir growth (e.g., Druitt et al., 2012).

ACKNOWLEDGMENTS

This work was funded by the Natural Environmental Research Council (NERC, grant NE/G01843X/1), two NERC-Geophysical Equipment Facility instrument loans (910 and 928), and the EC-FP7 VUELCO project (grant agreement 282759). M. Sunagua, SERGEOTECMIN, and SERNAP provided assistance in the field in Bolivia. The paper benefitted from thoughtful comments by two anonymous reviewers and guest associate editor Matthew Pritchard.

REFERENCES CITED

Blewitt, G., Kreemer, C., Hammond, W.C., and Gazeaux, J., 2016, MIDAS robust trend estimator for accurate GPS station velocities without step detection: Journal of Geophysical Research: Solid Earth, v. 121, p. 2054–2068, https://doi.org/10.1002/2015JB012552.

Comeau, M.J., Unsworth, M.J., and Cordell, D., 2016, New constraints on the magma distribution and composition beneath Volcán Uturuncu and the southern Bolivian Altiplano from magnetotelluric data: Geosphere, v. 12, p. 1391–1421, https://doi.org/10.1130/GES01277.1.

Corchete, V., Flores, D., and Oviedo, F., 2006, The first high-resolution gravimetric geoid for the Bolivian tableland: BOLGEO: Physics of the Earth and Planetary Interiors, v. 157, p. 250–256, https://doi.org/10.1016/j.pepi.2006.04.004.

del Potro, R., Díez, M., Blundy, J., Camacho, A.G., and Gottsmann, J., 2013, Diapiric ascent of silicic magma beneath the Bolivian Altiplano: Geophysical Research Letters, v. 40, p. 2044–2048, https://doi.org/10.1002/grl.50493.

de Silva, S.L., 1989, Altiplano-Puna volcanic complex of the central Andes: Geology, v. 17, p. 1102–1106, https://doi.org/10.1130/0091-7613(1989)017<1102:APVCOT>2.3.CO;2.

Druitt, T.H., Costa, F., Deloule, E., Dungan, M., and Scaillet, B., 2012, Decadal to monthly timescales of magma transfer and reservoir growth at a caldera volcano: Nature, v. 482, p. 77–80, https://doi.org/10.1038/nature10706.

Fialko, Y., and Pearse, J., 2012, Sombrero uplift above the Altiplano-Puna magma body: Evidence of a ballooning mid-crustal diapir: Science, v. 338, p. 250–252, https://doi.org/10.1126/science.1226358.

Finnegan, N.J., and Pritchard, M.E., 2009, Magnitude and duration of surface uplift above the Socorro magma body: Geology, v. 37, p. 231–234, https://doi.org/10.1130/G25132A.1.

Gottsmann, J., Blundy, J.D., Henderson, S., Pritchard, M.E., and Sparks, R.S.J., 2017, Thermomechanical modeling of the Altiplano-Puna deformation anomaly: Multiparameter insights into magma mush reorganization: Geosphere, v. 13, p. 1042–1065, https://doi.org/10.1130/GES01420.1.

Henderson, S.T., and Pritchard, M.E., 2013, Decadal volcanic deformation in the Central Andes Volcanic Zone revealed by InSAR time series: Geochemistry Geophysics Geosystems, v. 14, p. 1358–1374, https://doi.org/10.1002/ggge.20074.

Henderson, S.T., and Pritchard, M.E., 2017, Time-dependent deformation of Uturuncu Volcano, Bolivia, constrained by GPS and InSAR measurements and implications for source models: Geosphere, https://doi.org/10.1130/GES01203.1.

Hofmann-Wellenhof, B., and Moritz, H., 2005, Physical Geodesy: Vienna, Springer, 403 p.

Kern, J.M., de Silva, S.L., Schmitt, A.K., Kaiser, J.F., Iriarte, A.R., and Economos, R., 2016, Geochronological imaging of an episodically constructed subvolcanic batholith: U-Pb in zircon chronochemistry of the Altiplano-Puna Volcanic Complex of the Central Andes: Geosphere, v. 12, p. 1054–1077, https://doi.org/10.1130/GES01258.1.

Laumonier, M., Gaillard, F., Muir, D., Blundy, J., and Unsworth, M., 2017, Giant magmatic water reservoirs at mid-crustal depth inferred from electrical conductivity and the growth of the continental crust: Earth and Planetary Science Letters, v. 457, p. 173–180, https://doi.org/10.1016/j.epsl.2016.10.023.

Muir, D.D., Barfod, D.N., Blundy, J.D., Rust, A.C., Sparks, R.S.J., and Clarke, K.M, 2015, The temporal record of magmatism at Cerro Uturuncu, Bolivian Altiplano, *in* Caricchi, L., and Blundy, J.D., eds., Chemical, Physical and Temporal Evolution of Magmatic Systems: Geological Society of London Special Publication 422, p. 57–83, https://doi.org/10.1144/SP422.1.

Parker, A.L., Biggs, C.J., and Lu, Z., 2014, Investigating long-term subsidence at Medicine Lake Volcano, CA, using multitemporal InSAR: Geophysical Journal International, v. 199, p. 844–859, https://doi.org/10.1093/gji/ggu304.

Pearse, J., and Fialko, Y., 2010, Mechanics of active magmatic intraplating in the Rio Grande Rift near Socorro, New Mexico: Journal of Geophysical Research, v. 115, B07413, https://doi.org/10.1029/2009JB006592.

Perkins, J.P., Finnegan, N.J., Henderson, S.T., and Rittenour, T.M., 2016, Topographic constraints on magma accumulation below the actively uplifting Uturuncu and Lazufre volcanic centers in the Central Andes: Geosphere, v. 12, p. 1078–1096, https://doi.org/10.1130/GES01278.01271.

Pritchard, M.E., and Simons, M., 2002, A satellite geodetic survey of large-scale deformation of volcanic centres in the central Andes: Nature, v. 418, p. 167–171, https://doi.org/10.1038/nature00872.

Salisbury, M.J., Jicha, B.R., de Silva, S.L., Singer, B.S., Jimenez, N.C., and Ort, M.H., 2011, $^{40}Ar/^{39}Ar$ chronostratigraphy of Altiplano-Puna volcanic complex ignimbrites reveals the development of a major magmatic province: Geological Society of America Bulletin, v. 123, p. 821–840, https://doi.org/10.1130/B30280.1.

Sparks, R.S.J., Folkes, C.B., Humphreys, M.C.S., Barfod, D.N., Clavero, J., Sunagua, M.C., McNutt, S.R., and Pritchard, M.E., 2008, Uturuncu volcano, Bolivia: Volcanic unrest due to mid-crustal magma intrusion: American Journal of Science, v. 308, p. 727–769, https://doi.org/10.2475/06.2008.01.

Vanicek, P., Castle, R.O., and Balazs, E.I., 1980, Geodetic leveling and its applications: Reviews of Geophysics, v. 18, p. 505–524, https://doi.org/10.1029/RG018i002p00505.

Ward, K.M., Zandt, G., Beck, S.L., Christensen, D.H., and McFarlin, H., 2014, Seismic imaging of the magmatic underpinnings beneath the Altiplano-Puna volcanic complex from the joint inversion of surface wave dispersion and receiver functions: Earth and Planetary Science Letters, v. 404, p. 43–53, https://doi.org/10.1016/j.epsl.2014.07.022.

Zandt, G., Leidig, M., Chmielowski, J., Baumont, D., and Yuan, X., 2003, Seismic detection and characterization of the Altiplano-Puna magma body, central Andes: Pure and Applied Geophysics, v. 160, p. 789–807, https://doi.org/10.1007/PL00012557.